Research Article

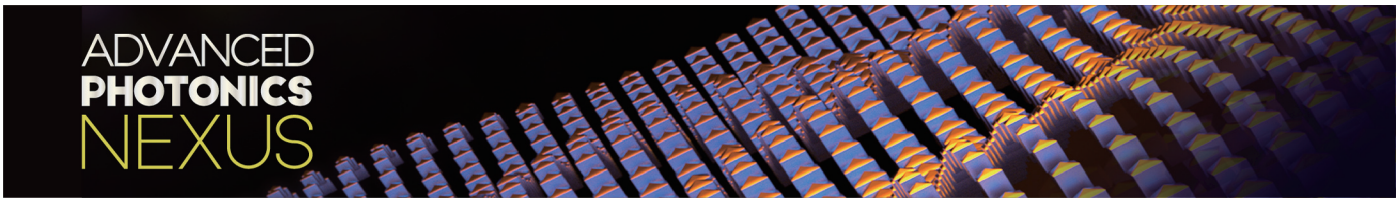

Electromagnetic modeling of interference, confocal, and focus variation microscopy

Tobias Pahl,* Felix Rosenthal, Johannes Breidenbach, Corvin Danzglock, Sebastian Hagemeier, Xin Xu, Marco Künne, and Peter Lehmann

University of Kassel, Faculty of Electrical Engineering and Computer Science, Measurement Technology Group, Kassel, Germany

Abstract. We present a unified electromagnetic modeling of coherence scanning interferometry, confocal microscopy, and focus variation microscopy as the most common techniques for surface topography inspection with micro- and nanometer resolution. The model aims at analyzing the instrument response and predicting systematic deviations. Since the main focus lies on the modeling of the microscopes, the light–surface interaction is considered, based on the Kirchhoff approximation extended to vectorial imaging theory. However, it can be replaced by rigorous methods without changing the microscope model. We demonstrate that all of the measuring instruments mentioned above can be modeled using the same theory with some adaption to the respective instrument. For validation, simulated results are confirmed by comparison with measurement results.

Keywords: interference microscopy; coherence scanning interferometry; confocal microscopy; focus variation microscopy; electromagnetic modeling; surface topography measurement.

Received Nov. 17, 2023; revised manuscript received Dec. 15, 2023; accepted for publication Dec. 27, 2023; published online Feb. 5, 2024.

[DOI: 10.1117/1.APN.3.1.016013]

1 Introduction

Optical surface topography measurement techniques, such as coherence scanning interferometry (CSI) being representative for interference microscopy, confocal microscopy (CM), and focus variation microscopy (FVM) are widespread for fast and contactless measurement of geometrical surface features, down to lateral dimensions of several 100 nm and an axial resolution down to the subnanometer range, depending on the respective measurement technique. All of the three named measurement methods show advantages compared to each other with respect to characteristics, such as axial resolution (CSI),[1,2] lateral resolution (CM),[3,4] or the capability of measuring steep slopes (FVM).[5,6] A detailed description of common surface topography measurement instruments is out of the scope of this paper but is provided in a book edited by Leach.[7] Further, it should be noted that besides surface topography inspection, measurement techniques as CSI or CM are also used in other fields of application, such as 3D imaging of biological samples. Several other familiar terms, such as white-light interferometry or optical coherence tomography, refer to CSI techniques.[1,8] Depending on the field of application parameters, such as the illumination wavelength or numerical aperture (NA) as well as the signal processing algorithm, can differ, leading to different specifications of system characteristics, such as the lateral or axial resolution. In this study, we focus on surface topography measurement techniques operating with light in the visible range.

Due to the wave properties of light and resulting diffraction effects, optical profilers always suffer from systematic deviations occurring with respect to certain surface characteristics and system parameters.[9–18] In order to predict and analyze these deviations, numerical models are developed. In this study, we present an extension of the vectorial Kirchhoff model introduced in former publications,[19,20] where inconsistencies are fixed and local reflection coefficients depending on the local surface slope are considered. The extended model is unified in a sense that it applies to CSI, CM, and FVM.

Generally, simulation models of optical surface profilers are either quasianalytic or rigorous models depending on the computation of the light scattering process. Usually, quasianalytic models require less computation time and memory. They also provide better physical insight in the imaging and scattering processes and are hence often preferred over rigorous models. On the other hand, rigorous simulations show higher accuracy,

*Address all correspondence to Tobias Pahl, tobias.pahl@uni-kassel.de

since no approximations are made. As the modeling of the measurement instruments is the main focus of this study, we concentrate on quasianalytic scattering theory. The scattering model, which describes the light–surface interaction, is usually independent of the instrument modeling and can therefore be changed if necessary. Further, surface textures typically measured by FVM may have geometrical dimensions that are too large to calculate scattered fields rigorously in reasonable time. Thus for rigorous modeling, we refer to previous publications for CSI[21] and CM.[22]

In the previous studies, quasianalytic models are developed based on Fourier optics or scalar Kirchhoff theory to analyze systematic deviations and the transfer characteristics of CSI systems,[15,23–26] confocal microscopes,[12,14,27] as well as conventional or FVM.[28–30]

It should be noted that with respect to the scattering surface, the so-called phase object approximation[15,19,27] and foil model[23,25,29] are based on the same scalar Kirchhoff scattering theory[31] and thus show similar results.[19,32] Generally, the phase object approximation is more flexible regarding incidence angle and surface material dependence of reflection coefficients and is less affected by numerical artifacts. As an additional advantage, the phase object approach can be simply exchanged by a rigorous method in the modeling of surface topography instruments if required, since both may be considered by a pupil integration. The foil model describes the surface as an infinitely thin foil-like object and considers the measurement process by a 3D convolution of the foil with the 3D point spread function (PSF) corresponding to the measurement instrument, which is calculated from the 3D transfer function (TF). Lehmann and Pahl[30] presented an analytic calculation of the 3D TF for conventional microscopes and CSI[33] enabling a fast computation of the 3D PSF. An extremely quick computation of CSI results is enabled by multiplying the 2D Fourier transform of the phase object with a cross section of the analytic 3D TF resulting in the scalar so-called universal Fourier optics (UFO) model.[34] A comparison of the so-called elementary Fourier optics model,[35] which is similar to the UFO model but approximates the cross section of the 3D TF by the conventional modulation transfer function, the UFO model, and the foil model is provided by Hooshmand et al.[32]

However, if imaging systems of high NA larger than 0.6 are applied, a vectorial treatment is appropriate, since polarization-dependent focusing and reflectivity become important, as mentioned by Totzeck.[36] Further, dark-field illumination, which is usually applied in FVM, implies large angles of incidence as well and hence requires a vectorial treatment. Due to the trend toward miniaturization of surface features, demands on the resolution of optical profilers increase continuously. Therefore, systems of high NA or additional dark-field illumination are being developed, leading to increasing challenges in modeling.

Rahlves et al.[14] presented a vectorial signal modeling of CM. However, lateral scanning, which is one major and time-consuming task in CM modeling, is not considered. Xie[27] developed a scalar model based on the vector theory of Richards and Wolf[37] describing the field in the focus of a microscope objective lens. Nonetheless, the model presented by Xie only considers the zeroth order of diffraction for depth scan, leading to significant disadvantages compared to the conventional Kirchhoff model as demonstrated in a previous study.[19] A vectorial extension of the scalar Kirchhoff model for CSI has been presented by Pahl et al.[19] However, the model shows inconsistencies, since the electric field is not perpendicular to the wave vector after the scattering process anymore. These inconsistencies are partially fixed in a recent publication.[20] Here the remaining inconsistencies are fixed and not only CSI, but also CM and FVM, are modeled similarly. For validation, results obtained from the vectorial model are compared to measurement results for all three instruments.

2 Model of Optical Imaging Profilometry

Generally, simulation models of microscopic arrangements can be split into three parts, illumination, light–surface interaction, and imaging as described by Totzeck.[36] Since the light–surface interaction and the microscopic imaging are similar for all three measurement techniques, we first focus on modeling the scattering and imaging process of plane waves scattered at the sample's surface. Afterward, we present the modeling of illumination and other properties, which differ among the measurement techniques. Further, we restrict the modeling to surface profiles that are invariant under translation in one dimension (here y) for reasons of simulation time, but the extension to 3D profiles is straightforward. Note that the modeling of illumination and imaging remains fully 3D. For the sake of completeness, the extensions, which need to be done to model 3D profiles, are briefly explained at the end of Sec. 2.1.2.

The models of the microscopic arrangements presented in this study are based on general integral formulations, which are numerically implemented by sums, and are used in the same way with rigorous scattering models. It should be noted that under certain circumstances faster implementations, such as the UFO model[34] for CSI exist, where properties of the measurement instruments are considered by analytically calculated 3D TFs. However, these specifications are based on the same theory, require a deeper understanding of the imaging system, and are more complicated to implement, especially if angle or material-dependent properties need to be considered.

2.1 Scattering Theory

The scattering theory presented by Beckmann[38] is a scalar theory based on the Kirchhoff approximation. However, in order to consider microscope objective lenses of high NA, a vectorial extension of the scattering model is required. Thus, we first present the scalar model and afterward show the vectorial extension.

2.1.1 Scalar model

In the scalar model, the electric object (o) field is restricted to a scalar field distribution $\psi_{\mathrm{o};k,\theta_{\mathrm{in}},\varphi_{\mathrm{in}}}$. Based on the Beckmann theory of scattering,[38] the scattered far-field distribution of a plane incident wave $\psi_{\mathrm{in};k,\theta_{\mathrm{in}},\varphi_{\mathrm{in}}} = \psi_0 \mathrm{e}^{\mathrm{i}\mathbf{k}_{\mathrm{in}}\cdot\mathbf{r}}$ of amplitude ψ_0 and wave vector

$$\mathbf{k}_{\mathrm{in}} = \begin{pmatrix} k_{\mathrm{in};x} \\ k_{\mathrm{in};y} \\ k_{\mathrm{in};z} \end{pmatrix} = k \begin{pmatrix} \sin\theta_{\mathrm{in}} \cos\varphi_{\mathrm{in}} \\ \sin\theta_{\mathrm{in}} \sin\varphi_{\mathrm{in}} \\ -\cos\theta_{\mathrm{in}} \end{pmatrix} \tag{1}$$

scattered by a phase object of height profile $h(x)$ is given by

$$\psi_{\mathrm{o};k,\theta_{\mathrm{in}},\varphi_{\mathrm{in}}}(x,z) = \psi_0 R(x,k,\theta_{\mathrm{in}},\varphi_{\mathrm{in}}) e^{\mathrm{i}[q_z(h(x)+z)+k_{\mathrm{in};x}x]}, \tag{2}$$

where $\mathbf{q} = (q_x, q_y, q_z)^{\mathrm{T}} = \mathbf{k}_{\mathrm{s}} - \mathbf{k}_{\mathrm{in}}$ with the scattered wave vector $\mathbf{k}_{\mathrm{s}}$. The incident angles θ_{in}, φ_{in} and scattering angles θ_{s},

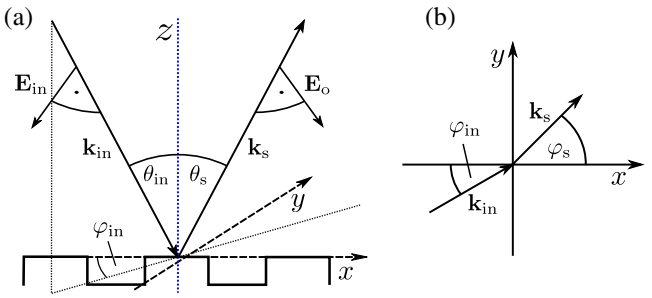

Fig. 1 Sketch of the scattering geometry including definitions of wave vectors, electric fields, and angles of incidence in (a) x–z plane and (b) x–y plane. The optical axis of the objective lens corresponds to the z-axis.

φ_s are defined in Fig. 1. $R(x, k, \theta_{in}, \varphi_{in})$ describes the Fresnel reflection coefficient of the surface depending on the wavenumber $k = 2\pi/\lambda$ with the wavelength λ of light illuminating the surface. Note that the average height $\overline{h}$ is defined to be zero, and the axial position $z = 0$ corresponds to the focal plane of the microscope. Generally, the variable z describes the axial displacement of the object from the focus position to consider depth scanning in the microscope models.

The general scattering theory derived by Beckmann[38] describes the scattered field by an integration over the area A of the scattering object, which corresponds to a Fourier transform approximating A to be sufficiently large. In this study, we focus on periodic surface profiles resulting in a Fourier series expansion instead of the Fourier transform. However, in general the theory is not restricted to periodic surface profiles, as nonperiodic surfaces can be considered using an appropriate window function. Further, it should be mentioned that the obliquity or inclination factors derived by Beckmann[38] are replaced by appropriate pupil functions according to the respective microscope arrangement.

Assuming a periodic surface profile $h(x)$ with period length L_x, i.e., periodic reflection coefficient $R(x, k, \theta_{in}, \varphi_{in})$, and considering the linear filtering process by the instrument, the field in the image plane of a microscope can be described by the Fourier series

$$\psi_{o;k,\theta_{in},\varphi_{in}}(x, z) = e^{ik_{in;x}x} \sum_{n=n_{min}}^{n_{max}} \sqrt{\frac{k_{s;z,n}}{k_{in;z}}}\, c_n e^{i2\pi nx/L_x - iq_{z,n}z}, \tag{3}$$

where

$$n_{min} = \frac{L_x}{\lambda}\left(-\sqrt{NA^2 - \frac{k_{in;y}^2}{k^2}} - \frac{k_{in;x}}{k}\right), \tag{4}$$

and

$$n_{max} = \frac{L_x}{\lambda}\left(\sqrt{NA^2 - \frac{k_{in;y}^2}{k^2}} - \frac{k_{in;x}}{k}\right) \tag{5}$$

are the minimum and maximum diffraction orders limited by the NA of the objective lens,[19] c_n is the Fourier coefficient related to the diffraction order n,[15] and the square root term considers energy conservation.[39]

2.1.2 Vectorial extension

If objective lenses of high NA or dark-field illumination are used, a vectorial treatment of the scattering process increases the accuracy of modeling. Hence, the scalar field distribution of Sec. 2.1.1 is extended to the vectorial electric field $\mathbf{E}_{o;k,\theta_{in},\varphi_{in}}$. In the case of vectorial modeling, rotations of the electric field occurring in the illumination, scattering process, and imaging are to be considered, since the electric field needs to be perpendicular to the corresponding wave vector. Here we mainly give the equations without detailed derivation. However, it should be noted that a similar scattered field equation can be derived based on the vectorial so-called Stratton–Chu integral. For more information, on the derivation of the vectorial scattering equations, we refer to Ref. 40. Therefore, the electric field is calculated by

$$\mathbf{E}_{o;k,\theta_{in},\varphi_{in}}(x, z) = e^{ik_{in;x}x} \sum_{n=n_{min}}^{n_{max}} \underline{R}^T(\theta_{s;n}, \varphi_{s;n})\underline{T}(\theta_{s;n}, \varphi_{s;n}) P_s(\theta_{s;n}, \varphi_{s;n}) \sqrt{\frac{k_{s;z,n}}{k_{in;z}}}\mathbf{c}_n e^{i2\pi nx/L_x - iq_{z,n}z}, \tag{6}$$

where

$$\underline{T}(\theta_{s;n}, \varphi_{s;n}) = \begin{pmatrix} \cos\theta_{mode,n} & -\sin\theta_{mode,n} \\ -\sin\theta_{mode,n} & -\cos\theta_{mode,n} \end{pmatrix}, \tag{7}$$

with

$$\theta_{mode,n} = \arcsin\left(\frac{k_{in;x}}{\sqrt{k^2 - k_{in;y}^2}}\right) - \arcsin\left(\frac{k_{s;x,n}}{\sqrt{k^2 - k_{s;y}^2}}\right) \tag{8}$$

representing a rotation matrix in the x–z plane, ensuring that the electric field remains perpendicular to the corresponding wave vector. $\underline{R}^T$ describes the rotation of the scattered electric field passing the objective lens and is the transpose of the matrix $\underline{R}$. In this context, it should be noted that the rotation of the electric field being focused on a camera is neglected due to large magnification factors.

$$\mathbf{c}_n = \frac{1}{L_x}\int_{-L_x/2}^{L_x/2} dx\, e^{-iq_{z,n}h(x)} e^{-i2\pi nx/L_x} [R_{\perp;k,\theta_{in},\varphi_{in}}(x)\mathbf{E}_{in,\perp;k,\theta_{in},\varphi_{in}}(x) + R_{\parallel;k,\theta_{in},\varphi_{in}}(x)\mathbf{E}_{in,\parallel;k,\theta_{in},\varphi_{in}}(x)] \tag{9}$$

is the vectorial Fourier coefficient, and P_s in Eq. (6) is a pupil function considering aberrations and apodization affecting the scattered field. The reflection coefficients $R_{\perp;k,\theta_{in},\varphi_{in}}$, $R_{\parallel;k,\theta_{in},\varphi_{in}}$ as well as the parts $\mathbf{E}_{in,\perp;k,\theta_{in},\varphi_{in}}$, $\mathbf{E}_{in,\parallel;k,\theta_{in},\varphi_{in}}$ of the incident electric field $\mathbf{E}_{in;k,\theta_{in},\varphi_{in}}$ perpendicular and parallel to the plane of incidence defined by the incident wave vector and the surface normal $\mathbf{n}(x) = [1 + m(x)^2]^{-0.5}[-m(x), 0, 1]^T$ vary with respect to the x axis due to the dependency of $\mathbf{n}$ on the local surface slope $m(x) = \partial h(x)/\partial x$ calculated based on the numerical derivative of $h(x)$. It should be noted that depolarization effects are

considered in the space- and slope-dependent parts of the electric field and the corresponding polarization-dependent reflection coefficients as described by Beckmann and Spezzichino.[38]

In order to split the incident field into parallel and perpendicular parts, the unit vectors $\mathbf{u}_{\parallel}$ and $\mathbf{u}_{\perp}$ parallel and perpendicular to the plane of incidence are given by

$$\mathbf{u}_{\parallel}(x)=\frac{\mathbf{k}_{\text{in}}\times\mathbf{n}(x)}{|\mathbf{k}_{\text{in}}\times\mathbf{n}(x)|}\quad\text{and}\quad\mathbf{u}_{\perp}(x)=\frac{\mathbf{k}_{\text{in}}\times(\mathbf{k}_{\text{in}}\times\mathbf{n}(x))}{|\mathbf{k}_{\text{in}}\times(\mathbf{k}_{\text{in}}\times\mathbf{n}(x))|}. \tag{10}$$

The components of the electric field are then given by

$$\begin{aligned}\mathbf{E}_{\text{in},\parallel;k,\theta_{\text{in}},\varphi_{\text{in}}}&=(\mathbf{E}_{\text{in};k,\theta_{\text{in}},\varphi_{\text{in}}}\cdot\mathbf{u}_{\parallel})\mathbf{u}_{\parallel}\quad\text{and}\\ \mathbf{E}_{\text{in},\perp;k,\theta_{\text{in}},\varphi_{\text{in}}}&=(\mathbf{E}_{\text{in};k,\theta_{\text{in}},\varphi_{\text{in}}}\cdot\mathbf{u}_{\perp})\mathbf{u}_{\perp}.\end{aligned} \tag{11}$$

In order to compute the incident electric field $\mathbf{E}_{\text{in};k,\theta_{\text{in}},\varphi_{\text{in}}}(\mathbf{r})=\underline{R}(\theta_{\text{in}},\varphi_{\text{in}})\mathbf{E}_0e^{i\mathbf{k}_{\text{in}}\cdot\mathbf{r}}$, the initial polarization vector $\mathbf{E}_0$ describing the incident field before being focused is multiplied by the rotation matrix,

$$\underline{\mathbf{R}}(\theta_{\text{in}},\varphi_{\text{in}})=\begin{pmatrix}\cos^2\varphi_{\text{in}}\cos\theta_{\text{in}}+\sin^2\varphi_{\text{in}} & \sin\varphi_{\text{in}}\cos\varphi_{\text{in}}(\cos\theta_{\text{in}}-1)\\ \sin\varphi_{\text{in}}\cos\varphi_{\text{in}}(\cos\theta_{\text{in}}-1) & \sin^2\varphi_{\text{in}}\cos\theta_{\text{in}}+\cos^2\varphi_{\text{in}}\\ \sin\theta_{\text{in}}\cos\varphi_{\text{in}} & \sin\theta_{\text{in}}\sin\varphi_{\text{in}}\end{pmatrix}, \tag{12}$$

considering the rotation of the field due to focusing.[22]

It should be mentioned that the Kirchhoff theory is limited to surface profiles with radii of curvature, which are large compared to the wavelength of light,[31,38,41] and effects such as multiple scattering, polarization-dependent diffraction, and shadowing are not considered. Further studies on the validity of the Kirchhoff approximation are given by Thorsos[42] and Thorsos and Jackson.[43] However, if the validity of the Kirchhoff approximation is not given, the Fourier coefficients [see Eq. (9)] can be calculated rigorously using FEM for scalar[44] and vectorial[21,22] coefficients, with the drawback of long computation time and large computer memory requirements. Therefore, the implementation is performed in a way that the scattered field computation method can be changed without changing the modeling of the imaging technique.

For 3D surface profiles, the Fourier series [Eq. (3) for scalar and Eq. (6) for vectorial] needs to be calculated depending on two spatial coordinates, x and y, and hence, the diffraction orders are defined by two numbers, n and m. Therefore, the limits of the diffraction orders [Eqs. (4) and (5)] are changed to limits for n and m fulfilling the condition $k_{\text{s};x,n,m}^2+k_{\text{s};y,n,m}^2\leq k^2\text{NA}^2$. In case of the scalar modeling, these are the only adjustments that need to be done. For the vectorial model, the extension is slightly more complicated, since further changes are required in the rotation of the electric field to ensure that the electric field remains perpendicular to the wave vector of the respective mode. Further, the local normal to surface and therewith the reflection coefficients depend on x and y. However, the procedure is quite similar to the presented model for 2D surfaces and thus the extension is straightforward.

2.2 Microscope Models

The scattered electric field for plane wave illumination can be calculated according to Eq. (6) for all of the presented instruments. However, there are effects, such as coherence and interference, that need to be considered, depending on the measurement method. Note that aberrations, apodization, and inhomogeneous illumination can be simply considered by pupil functions as described in Refs. 21 and 22 but are neglected in this study for simplicity if not explicitly mentioned otherwise.

2.2.1 Coherence scanning interferometry

A schematic representation of a coherence scanning interferometer in Linnik configuration is shown in Fig. 2(a). Note that there

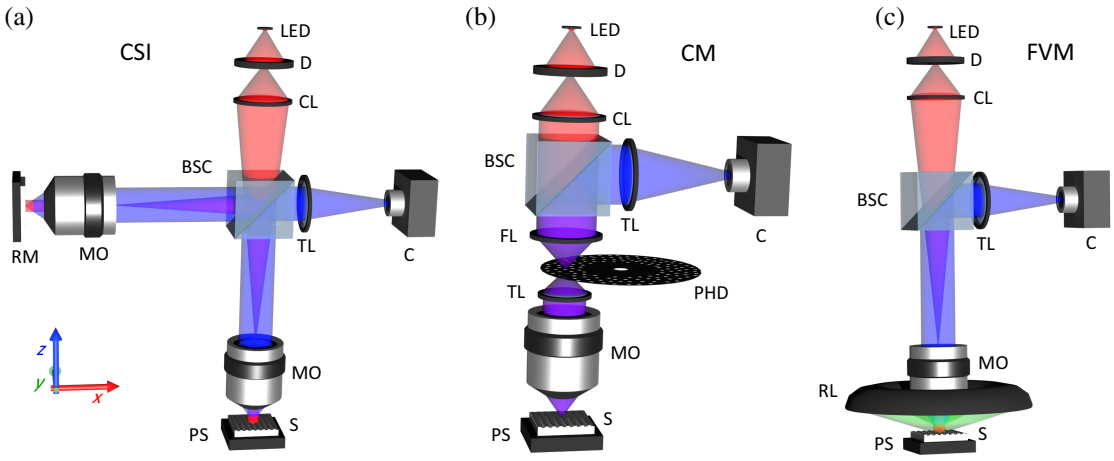

Fig. 2 Schematic representations of (a) a coherence scanning interferometer in Linnik configuration, (b) a confocal microscope with spinning disk for lateral scanning, and (c) a focus variation microscope with ring light illumination. The illumination beam path is sketched in red (bright-field), the imaging beam path in blue, and the dark-field ring light (RL) is shown in green in the case of FVM. D, diffuser; CL, condenser lens; RM, reference mirror; MO, microscope objective; BSC, beam splitter cube; TL, tube lens; C, camera; PS, piezo stage; S, sample; PHD, pinhole disk; and FL, field lens.

are other frequently used CSI arrangements, such as Michelson or Mirau configurations, the modeling of which is similar. The illumination beam path sketched in the figure in red corresponds to Köhler illumination.[3] Hence, a spatially extended light source represented by the diffuser is imaged in the back focal plane of the objective lenses leading to plane incident waves of certain angles of incidence with respect to the object and the reference mirror. Therefore, each plane wave incident under a certain angle originates from another point of the light source and, thus, the illumination is spatially incoherent. As a consequence, the intensity $I_{k,\theta_{\mathrm{in}},\varphi_{\mathrm{in}}}(x,z) \sim |\mathbf{E}_{\mathrm{o};k,\theta_{\mathrm{in}},\varphi_{\mathrm{in}}}(x,z) + \mathbf{E}_{\mathrm{ref};k,\theta_{\mathrm{in}},\varphi_{\mathrm{in}}}(x)|^2$, with the reference field $\mathbf{E}_{\mathrm{ref};k,\theta_{\mathrm{in}},\varphi_{\mathrm{in}}}(x)$ obtained from reflection at a plane surface, superimposes on the camera for various angles of incidence. The intensity I_k for monochromatic illumination is thus given by[19]

$$I_k(x,z) \sim \int_0^{2\pi} \mathrm{d}\varphi_{\mathrm{in}} \int_{\theta_{\min}}^{\theta_{\max}} \mathrm{d}\theta_{\mathrm{in}} P_{\mathrm{in}}(\theta_{\mathrm{in}},\varphi_{\mathrm{in}})^2 I_{k,\theta_{\mathrm{in}},\varphi_{\mathrm{in}}}(x,z) \sin\theta_{\mathrm{in}} \cos\theta_{\mathrm{in}}, \tag{13}$$

with the angles of incidence as defined in Fig. 1. $\theta_{\min}$ is the minimum incident angle,[21] which equals zero for Linnik and Michelson configurations, $\theta_{\max} = \arcsin(\mathrm{NA})$, and $P_{\mathrm{in}}(\theta_{\mathrm{in}},\varphi_{\mathrm{in}})$ is the pupil function affecting the incident electric field considering apodization, aberrations, and inhomogeneous illumination. Note that in case of Mirau configuration, the scattered field also needs to be filtered in a way that the scattering angle is larger than $\theta_{\min}$. Further, it should be mentioned that often only the interference intensity $I_{\mathrm{int};k,\theta_{\mathrm{in}},\varphi_{\mathrm{in}}} \sim \mathrm{Re}\{\mathbf{E}_{\mathrm{o};k,\theta_{\mathrm{in}},\varphi_{\mathrm{in}}}(x,z) \cdot \mathbf{E}^*_{\mathrm{ref};k,\theta_{\mathrm{in}},\varphi_{\mathrm{in}}}(x)\}$ with the complex conjugated reference field $\mathbf{E}^*_{\mathrm{ref};k,\theta_{\mathrm{in}},\varphi_{\mathrm{in}}}$ is considered in CSI simulations. However, for profiles, which significantly influence the field's amplitude during axial scanning, it is more convenient to calculate the complete intensity instead of only the interference component.

For a polychromatic light source with the spectrum $S(k)$, the measured intensity is given by integration

$$I(x,z) \sim \int_0^{\infty} \mathrm{d}k\, F(k) S(k) I_k(x,z), \tag{14}$$

where $F(k)$ describes the spectral sensitivity of the camera. $I(x,z)$ is the intensity, which would be recorded by the camera during a depth scan in real measurements. Further, the intensity is averaged over the pixel area of the respective camera.

2.2.2 Confocal microscopy

A schematic representation of a confocal microscope is displayed in Fig. 2(b). Compared to CSI, a rotating pinhole disc is placed in the illumination as well as in the imaging beam path. The pinholes in the illumination path can be considered as single-point sources emitting spatially coherent light. Since only small spots on the object's surface are illuminated by these pinholes, the pinhole disk rotates, leading to a lateral scanning of the measured surface section. The lateral scan can be considered in the simulation describing the field from a single pinhole, which is incident on the surface, in the pinhole plane by a δ function $\delta(x - x_0)$, where x_0 describes the position of the pinhole. Hence, the incident field in the Fourier plane is multiplied by a phase term depending on the pinhole position and leading to the incident field

$$\mathbf{E}_{\mathrm{in};k,\theta_{\mathrm{in}},\varphi_{\mathrm{in}}}(x,z,x_0) = \mathrm{e}^{-\mathrm{i}k_{\mathrm{in};x}x_0} \underline{R}(\theta_{\mathrm{in}},\varphi_{\mathrm{in}}) \mathbf{E}_0 \mathrm{e}^{\mathrm{i}\mathbf{k}_{\mathrm{in}}\cdot\mathbf{r}} \tag{15}$$

in the object plane. Due to spatial coherence, the electric fields related to different angles of incidence superimpose, leading to the total electric field

$$\mathbf{E}_{\mathrm{tot};k}(x,z,x_0) \sim \int_0^{2\pi} \mathrm{d}\varphi_{\mathrm{in}} \int_0^{\theta_{\max}} \mathrm{d}\theta_{\mathrm{in}} \mathbf{E}_{\mathrm{o};k,\theta_{\mathrm{in}},\varphi_{\mathrm{in}}}(x,z) P_{\mathrm{in}}(\theta_{\mathrm{in}},\varphi_{\mathrm{in}}) \sin\theta_{\mathrm{in}} \cos\theta_{\mathrm{in}} \mathrm{e}^{-\mathrm{i}k_{\mathrm{in};x}x_0} \tag{16}$$

and the corresponding intensity $I_k(x,z,x_0) \sim |\mathbf{E}_{\mathrm{tot};k}(x,z,x_0)|^2$, in contrast to CSI, where the intensities related to different angles of incidence superimpose [see Eq. (13)]. For more details on the modeling of the incident wave and lateral scanning, we refer Ref. 22.

Considering infinitely small pinholes or a spatially coherently illuminated pinhole disk, we can set $x_0 = x$. Thus the phase term following from lateral scanning in Eq. (16) and the phase term in front of the sum in Eq. (6) cancel out. If a pinhole disk of realistic size with radius ϱ is illuminated by spatially coherent light, this can be considered by multiplication of the incident field with

$$\tilde{\Theta}(k_{\mathrm{in};\rho}) = \frac{2\pi\varrho}{k_{\mathrm{in};\rho} M_{\mathrm{obj}}} J_1\left(\frac{k_{\mathrm{in};\rho}\varrho}{M_{\mathrm{obj}}}\right) \tag{17}$$

in the pupil plane, where $k_{\mathrm{in};\rho} = \sqrt{k_{\mathrm{in};x}^2 + k_{\mathrm{in};y}^2}$ and M_{obj} is the magnification of the objective lens. Note that $\tilde{\Theta}(k_{\mathrm{in};\rho})$ corresponds to the Fourier transform of a circular pinhole of radius ϱ. Similarly, the scattered field needs to be multiplied by $\tilde{\Theta}(k_{\mathrm{s};\rho})$. In the case of a spatially incoherently illuminated pinhole, the intensity needs to be calculated for certain positions $\tilde{x}_0$ within the pinhole around x_0 to average the intensity, while the imaging of the scattered field remains spatially coherent. However, this study assumes infinitely small pinholes. If polychromatic illumination is used, the total intensity follows from the integration similar to Eq. (14).

2.2.3 Focus variation microscopy

A schematic of a focus variation microscope is shown in Fig. 2(c). Similar to CSI, the bright-field illumination corresponds to Köhler illumination. Therefore, the total intensity is given by integration over all intensities obtained for plane incident waves within the NA of the objective lens, as shown in Eq. (13). Since no reference mirror exists, the intensity $I_{\mathrm{bf};k}(x,z)$ for bright-field illumination is given by

$$I_{\mathrm{bf};k}(x,z) \sim \int_0^{2\pi} \mathrm{d}\varphi_{\mathrm{in}} \int_0^{\theta_{\max}} \mathrm{d}\theta_{\mathrm{in}}\, P_{\mathrm{in}}(\theta_{\mathrm{in}},\varphi_{\mathrm{in}})^2 I_{k,\theta_{\mathrm{in}},\varphi_{\mathrm{in}}}(x,z) \sin\theta_{\mathrm{in}} \cos\theta_{\mathrm{in}}, \tag{18}$$

where $I_{k,\theta_{\mathrm{in}},\varphi_{\mathrm{in}}}(x,z) = |\mathbf{E}_{\mathrm{o};k,\theta_{\mathrm{in}},\varphi_{\mathrm{in}}}(x,z)|^2$. In addition to the bright-field illumination, FVM often uses additional dark-field illumination, sketched in Fig. 2(c) in green and referred to as ring light in order to get information on steeply sloped surfaces. The intensity $I_{\mathrm{df};k}(x,z)$ obtained from dark-field illumination is calculated by

$$I_{\mathrm{df};k}(x,z) \sim \int_0^{2\pi} \mathrm{d}\varphi_{\mathrm{in}} \int_{\theta_{\mathrm{df,min}}}^{\theta_{\mathrm{df,max}}} \mathrm{d}\theta_{\mathrm{in}}\, P_{\mathrm{in,df}}(\theta_{\mathrm{in}},\varphi_{\mathrm{in}})^2 \, I_{k,\theta_{\mathrm{in}},\varphi_{\mathrm{in}}}(x,z)\sin\theta_{\mathrm{in}}\cos\theta_{\mathrm{in}}, \tag{19}$$

where $\theta_{\mathrm{df,min}}$ and $\theta_{\mathrm{df,max}}$ are the minimum and maximum angles of incidence of the ring light. $P_{\mathrm{in,df}}(\theta_{\mathrm{in}},\varphi_{\mathrm{in}})$ is the pupil function for ring light illumination. The spectra in case of polychromatic light can be considered similar to Eq. (14), where the bright-field and dark-field illumination can have different spectra. The total intensity obtained by a camera is given by superposition, i.e., $I(x,z) = I_{\mathrm{bf}}(x,z) + I_{\mathrm{df}}(x,z)$. Thus, it should be noted that the correct weighting of the spectra should be considered before superposition.

3 Results

To validate the simulation model, results are exemplarily compared to measurement results obtained by CSI, CM, and FVM. As an example, sinusoidal surface profiles fulfilling the validity conditions of the Kirchhoff approximation will be examined. On the one hand, measurements of sinusoidal surfaces may show systematic deviations;[2,21] and on the other hand, the definition of the instrument transfer function (ITF), used for characterization of topography measurement instruments, is based on the measurement of sinusoidal surface topographies.[35] Hence, a precise modeling of the topography measurement process of sinusoidal surfaces is of particular interest. For CSI and CM, a sinusoidal standard (Rubert 543[45]) with period length $L_x = 2.5\ \mu$m and peak-to-valley (PV) height $h = 120$ nm is measured, and results are reproduced by simulation. FVM simulation results are validated using the Rubert 525 sinusoidal standard[45] with $L_x = 135\ \mu$m and $h = 19\ \mu$m, since longer periods and surface heights are generally required for reliable FVM measurements. For comparison, the profiles are measured by an atomic force microscope (AFM) with tip radius of 10 nm (Tap190Al-G probe tip[46]). Additionally, the Rubert 525 standard is measured by a tactile stylus instrument. Both instruments are described in detail by Hagemeier et al.[18,47] The spectra of the LED light sources used for the simulations are obtained by spectrometer measurements shown elsewhere.[15] Since the illuminating light is unpolarized, simulations are performed for TE [$\mathbf{E}_0 = (0,1)^{\mathrm{T}}$] as well as TM [$\mathbf{E}_0 = (1,0)^{\mathrm{T}}$] polarized light (see Sec. 2.1.2), and the resulting intensities are averaged. The simulations are performed using 70 different values for θ_{in}, 120 values for φ_{in}, and 9 different wavelength values.

It should be mentioned that simulations are validated by comparison with cross sections of 3D topography measurements in the xz plane for better visibility. The 3D surface topographies for the two CSI and the CM measurements are shown in Fig. 8 in the Appendix. The FVM result is not shown due to the low roughness of the specular surface, leading to large outliers in the measured surface topography.

It should be mentioned that we focus on an exemplary comparison between simulation and measurement to demonstrate that typical effects in optical surface topography measurement are reliably reproduced by the presented simulation model. Since the modeling of four different measurement instruments already requires a lot of explanation, a more general comparison is outside the scope of the paper. In order to underline the requirement of vectorial modeling, a comparison between results simulated using the vectorial and the scalar approach is shown exemplarily for CM in Fig. 9 in the Appendix.

3.1 Coherence Scanning Interferometry

CSI results are obtained using a 50× Mirau interferometer of NA = 0.55 with red LED illumination of central wavelength $\lambda_{\mathrm{c}} = 630$ nm and spectral full width at half-maximum (FWHM) of 17 nm. The radius r_{ref} of the reference mirror is estimated to be 0.35 mm, since no exact value is provided by the manufacturer. The width of a camera pixel amounts to 5.5 μm, and the spectral sensitivity of the camera is considered to be constant in the spectral range of the light source. The refractive index $n_{\mathrm{Ni}}(\lambda = 630\ \mathrm{nm}) = 1.2845 + 6.3329\mathrm{i}$[48] of the measurement object made of nickel is assumed to be constant for the spectrum of the LED light source. The material of the reference mirror is aluminum, with approximately constant $n_{\mathrm{Al}}(\lambda = 630\ \mathrm{nm}) = 0.8354 + 6.0385\mathrm{i}$.[49]

A simulated image stack related to a single camera line is shown in Fig. 3(a); the corresponding measurement result is displayed in Fig. 3(b). Note that after offset subtraction, the intensities are normalized by the maximum intensity. The z coordinate is related to the displacement of the sample from the balanced position and, thus a shift of an interference intensity maximum to higher z values leads to a lower height in the reconstructed surface profile.

Figures 3(a) and 3(b) show good agreement. Both patterns are sinusoidally modulated with respect to the lateral x coordinate following from the sinusoidal surface. Further, both results show an amplitude modulation with regard to the axial z coordinate. The signal's envelope results from temporal coherence related to the spectral width of the light source and the limited depth of field (also referred to as longitudinal spatial coherence)[50] due to the NA of the objective lens.

Surfaces are reconstructed using conventional CSI signal processing algorithms.[2,51] The result of the analysis of the

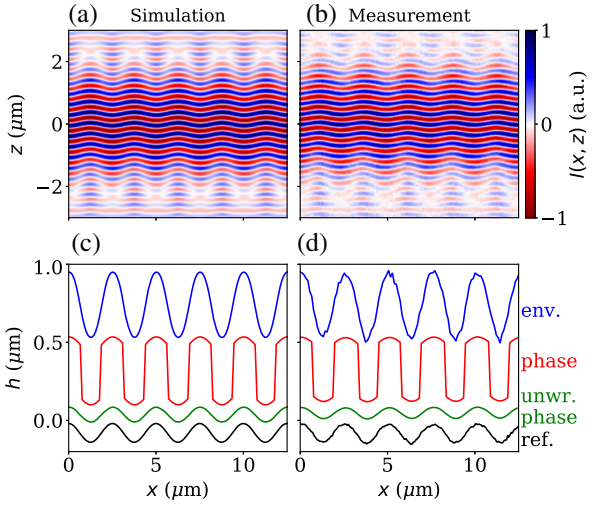

Fig. 3 (a), (c) Simulated and (b), (d) measured results for a sinusoidal surface profile of period length $L_x = 2.5\ \mu$m and PV height $h = 120$ nm obtained by a 50× Mirau interferometer of NA = 0.55 with red LED illumination; (a) and (b) show the offset reduced, normalized intensity obtained by depth scan, and surface profiles obtained by envelope (env.) and phase (phase) analysis are displayed in (c) and (d). Since the phase profiles suffer from phase jumps, the unwrapped phase (unwr. phase) profiles are plotted as well. For reference (ref.), a profile measured by AFM is presented in (d) and the nominal profile is presented in (c).

envelope's maximum position is named envelope profile, and the result obtained by phase analysis combined with fringe order detection using the envelope is referred to as phase profile. Reconstructed sinusoidal profiles obtained from simulation and measurement are presented in Figs. 3(c) and 3(d). In both figures, the reference profile, which is given by the nominal profile for simulation and by an AFM measurement result in the experimental case, is shown in black for comparison. The evaluation wavelength λ_{eval}[26] used for phase analysis is 680 nm.

The simulated as well as measured envelope profiles show an amplitude that is more than 3.5 times larger compared to the nominal PV amplitude of $h \simeq 120$ nm. Similar results are obtained by FEM simulation.[21] The enlarged measured amplitude can be explained by the implementation of envelope peak detection and the 3D transfer behavior of CSI characterized by the 3D TF.[33]

Due to the overestimation of the envelope profile's amplitude, the phase profiles suffer from phase jumps, which follow from an incorrect estimation of the fringe order through the envelope detection.[2] In order to get rid of these phase jumps, an unwrapping procedure is applied, leading to the profiles shown in green. For measurement and simulation, the amplitudes of the unwrapped phase profiles are smaller compared to the nominal height, which is consistent with expectations derived from the 3D TF[33] and from known ITFs[35] defined in particular by the output amplitude of a measured sinusoidal profile normalized by the real amplitude.

In order to verify simulation results for microscope arrangements of high lateral resolution, Fig. 4 shows simulated [Figs. 4(a) and 4(c)] and measured [Figs. 4(b) and 4(d)] results of the same sinusoidal standard measured by a 100× Linnik interferometer as sketched in Fig. 2(a) of NA = 0.95, with royal blue LED illumination of $\lambda_c = 440$ nm and FWHM = 24 nm. The refractive indices are similar to the Mirau simulation assumed

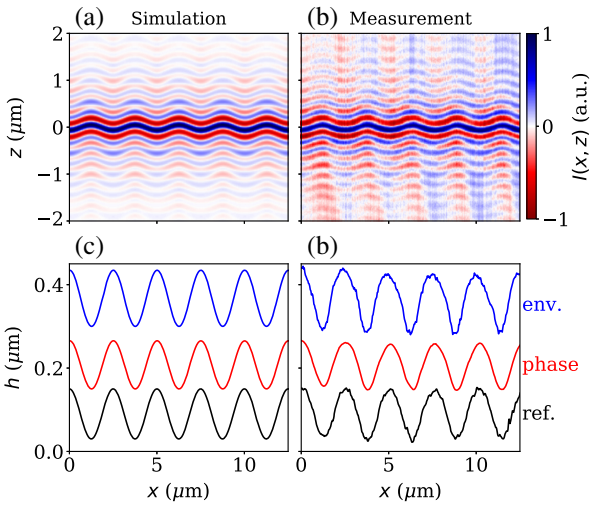

Fig. 4 (a), (c) Simulated and (b), (d) measured results from a sinusoidal surface profile of period length $L_x = 2.5$ μm and PV height $h = 120$ nm obtained by a 100× Linnik interferometer of NA = 0.95 with royal blue LED illumination. (a) and (b) show the offset reduced, normalized intensities depending on the depth scanner position, and surface profiles obtained by envelope (env.) and phase (phase) analysis are displayed in (c) and (d). For reference (ref.), a profile measured by an AFM is presented in (d) and the nominal profile is presented in (c).

to be constant over the spectral width of the light source, with $n_{Ni}(\lambda = 440\ \text{nm}) = 1.1829 + 3.6259i$[48] for the object and $n_{Ag}(\lambda = 440\ \text{nm}) = 0.4616 + 2.6133i$[48] for the reference mirror made of silver. The pixel width is 3.45 μm, and the sensitivity is assumed to be constant over the spectral width of the light source.

As expected, due to the higher NA and the resulting smaller depth of field[52] resulting in a limited longitudinal spatial coherence,[50] the envelope in both simulated and measured interference signals [see Figs. 4(a) and 4(b)] is narrower compared to the envelopes for NA = 0.55 (see Fig. 3). Again the phase modulation following from the sinusoidal surface structure can be obtained in both figures. Comparing Figs. 4(a) and 4(b), simulated and measured intensities show generally good agreement. Also, the behavior beyond the focal plane is quite similar. However, there are slight deviations between measured and simulated signals, which are more significant compared to the results of Fig. 3 for a smaller NA and Mirau configuration.

In this context, it should be noted that setting up and adjusting a Linnik interferometer, especially of high NA, is much more challenging than building Mirau or Michelson interferometers. The Linnik configuration requires two objective lenses that are assumed to be identical but are not fulfilled in reality. In addition, both objectives have to be placed at the same distance from the beam splitter cube and adjusted with respect to the optical axis. Due to the high NA and the small depth of field, even small deviations from the ideal adjustment cause deviations in the measurement results. Therefore, deviations obtained between the simulated and measured results probably follow from slight, inevitable misalignment and objective or beam splitter mismatch, finally leading to deviations in measured results. Analyzing the influence of maladjustment and aberrations on simulated results is outside the scope of this study but can be principally included in the simulation model by appropriate pupil functions, as shown elsewhere.[3,53,54]

Figures 4(c) and 4(d) display envelope and phase ($\lambda_{eval} = 600$ nm) profiles as well as the nominal surface used for simulation and an AFM profile as a reference. Due to the high NA of the Linnik interferometer, the amplitudes of both the envelope and the phase profiles correspond to the nominal amplitude, in contrast to the results according to Fig. 3. Further, simulated and measured profiles show good agreement. Slight deviations can be explained with the deviation of the real profile from an ideal sinusoid, which is verified by a comparison of both reference profiles. In addition, the microroughness of the Rubert standard[45] appears in the AFM as well as the envelope result, whereas the phase result is smoothed in Fig. 4(d). This effect is in agreement with previous observations.[18,33] Due to the high NA of the interferometer, the high-frequency roughness is reproduced in the measurement result. Thus the microroughness superimposing the sinusoidal profile leads to slightly larger deviations between simulation and measurement for high-NA CSI systems. Note that besides aberrations, these discrepancies between the ideal object geometry in the simulation and the real object additionally lead to slight deviations between Figs. 4(a) and 4(b).

Nonetheless, measurement results for both the Mirau and the Linnik interferometer are reliably reproduced by the simulation.

3.2 Confocal Microscopy

Results of a confocal microscope as sketched in Fig. 2(b) are simulated for a 100× microscope objective lens of NA = 0.95. For simplicity, the pinhole is assumed to be infinitely small.

However, comparing the width of modeled and measured confocal depth responses, the pupil functions [cf., Eqs. (6) and (16)] are assumed to be $P_{\text{in}}(\theta_{\text{in}}, \varphi_{\text{in}}) = \sqrt{\cos\theta_{\text{in}}}$ and $P_{\text{s}}(\theta_{\text{s}}, \varphi_{\text{s}}) = \sqrt{\cos\theta_{\text{s}}}$ considering apodization and approximately a finite pinhole size, since the exact pinhole size is not known and both effects behave similarly to low-pass filters. For a more detailed analysis of the influence of pupil functions and a finite pinhole size on simulation results, we refer to a previous study.[22]

Figure 5 shows CM results obtained again from the sinusoidal surface standard (Rubert 543) using a cyan light source of $\lambda_{\text{c}} = 500$ nm and FWHM $= 35$ nm. The refractive index is assumed to be $n_{\text{Ni}}(\lambda = 500\ \text{nm}) = 1.0496 + 4.4596\text{i}$[48] constantly over the spectral width, similar to the camera sensitivity. The pixel width of the camera is given 16 μm, considering the magnification of imaging the pinhole onto the camera (see Ref. 18).

Figure 5 displays simulated [Fig. 5(a)] and measured [Fig. 5(b)] intensity signals depending on the lateral x coordinate and the z position of the depth scanner. The intensity signals normalized by the maximum intensity value show good agreement. Both intensities are modulated by the sinusoidal shape of the object's surface and show a limited depth of field, which is additionally restricted by the confocal effect.

For better comparability, cross sections at fixed x positions marked by vertical lines in Figs. 5(a) and 5(b) are extracted and presented in Fig. 5(c). The signals obtained from the slopes of the profile are added to an offset intensity of 0.5 for better visibility. Simulated results shown by solid lines agree with the dashed lines representing measured depth responses. The intensities extracted at the slope show a slight reduction in the maximum intensity due to the loss of signal, which can be obtained similarly in simulation and measurement. In addition, signals captured from a locally flat surface section exhibit a slight asymmetry due to diffraction. This asymmetry is reproduced reliably in the simulated result.

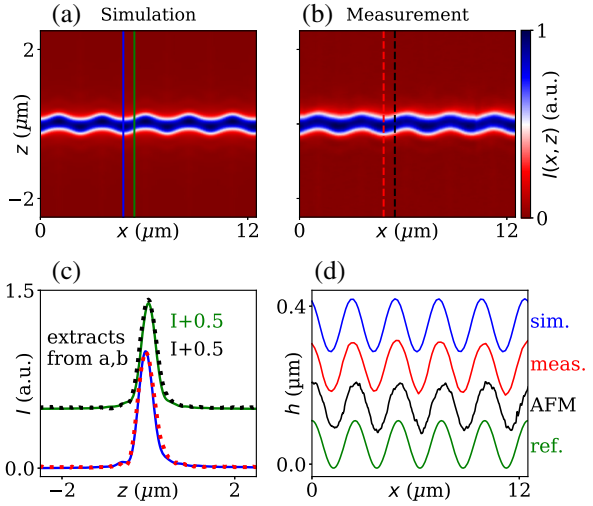

Fig. 5 (a) Simulated and (b) measured intensity responses obtained from a sinusoidal surface profile of period length $L_x = 2.5$ μm and PV height $h = 120$ nm considering a 100× NA $= 0.95$ confocal microscope with cyan LED illumination; vertical cross sections of (a) and (b) are plotted in (c) for comparison. The x positions, where the cross sections are extracted, are marked by lines of corresponding color and style in (a) and (b). Intensity signals obtained from a slope of the profile are raised by an offset of 0.5 for better visibility. (d) Profile reconstructions obtained from simulation (sim.), confocal measurement (meas.), and AFM measurement. The nominal reference (ref.) profile used for the simulation is plotted as well.

Profiles reconstructed by Gaussian approximation[18] are displayed in Fig. 5(d). For reference, a profile measured by an AFM and the nominal surface profile are additionally shown. The PV amplitudes correspond to the nominal amplitude for both measured and simulated profiles. Due to the larger pixel width of the camera compared to the CSI setup, the surface's microroughness is no longer present in the measured result.

In sum, measured and simulated intensities as well as evaluated profiles show good agreement.

3.3 Focus Variation Microscopy

FVM results are obtained for a 10× microscope objective lens of NA $= 0.45$. The bright-field illumination is implemented using green LED light of $\lambda_{\text{c}} = 535$ nm and FWHM $= 37$ nm. The red LED ($\lambda_{\text{c}} = 630$ nm, FWHM $= 17$ nm) dark-field illumination is applied with $\theta_{\text{df,min}} = 50°$ and $\theta_{\text{df,max}} = 79°$ placed on a ring around the microscope objective, as sketched in Fig. 2(c). The pixel width amounts to 4.65 μm. The setup is described in more detail by Xu et al.[17] As the lenses of the measurement setup suffer from apodization, again the pupil functions are chosen to be $P_{\text{in}}(\theta_{\text{in}}, \varphi_{\text{in}}) = \sqrt{\cos\theta_{\text{in}}}$ and $P_{\text{s}}(\theta_{\text{s}}, \varphi_{\text{s}}) = \sqrt{\cos\theta_{\text{s}}}$ in simulation. Similarly, due to the ring shape of the dark-field illumination, $P_{\text{in,df}}(\theta_{\text{in}}, \varphi_{\text{in}}) = \sqrt{\cos\theta_{\text{in}}}$ is assumed.

Since the axial resolution of focus variation microscopes is in the range of micrometers, a Rubert 525 sinusoidal standard[45] is examined. It should be noted that usually rough surfaces are required to achieve reliable FVM results. However, for comparison and validation of the simulation model, it is more reasonable to use a specular surface with deterministic texture. The influence of an additional microroughness superimposing the deterministic sinusoidal surface is demonstrated in simulation later in this section. Measurements and simulations are performed using only bright-field, only dark-field, and combined illumination to study the impact of both illumination types separately. The refractive index of nickel is assumed to be constantly $n_{\text{Ni}}(\lambda = 535\ \text{nm}) = 1.0676 + 4.9613\text{i}$ and $n_{\text{Ni}}(\lambda = 630\ \text{nm}) = 1.2845 + 6.3329\text{i}$.[48] Furthermore, the camera sensitivity is approximated to be constant due to the narrow spectral widths of the light sources. Apart from the spectral sensitivity, the ratio between the intensities of bright- and dark-field illumination needs to be adjusted anyway.

Figure 6 displays simulated [Figs. 6(a), 6(c), and 6(e)] and measured [Figs. 6(b), 6(d), and 6(f)] normalized intensities obtained by depth scans. Comparison between simulated and measured results shows good agreement for all three illumination configurations. In case of only bright-field illumination [Figs. 6(a) and 6(b)], bright spots from the peaks and valleys of the surface appear in the focus of the objective lens. Out of focus, the bright spots blur as expected. Almost no information is captured by the camera from the slopes of the surface due to the limited NA of the objective lens, which can be seen by the dark spots between the bright spots.

Compared to bright-field illumination, results obtained with dark-field illumination show maximum intensities at the slopes of the profile in focus. This observation meets the expectation, since specular reflection occurs at the peaks and valleys, and hence this light is not captured by the objective lens for

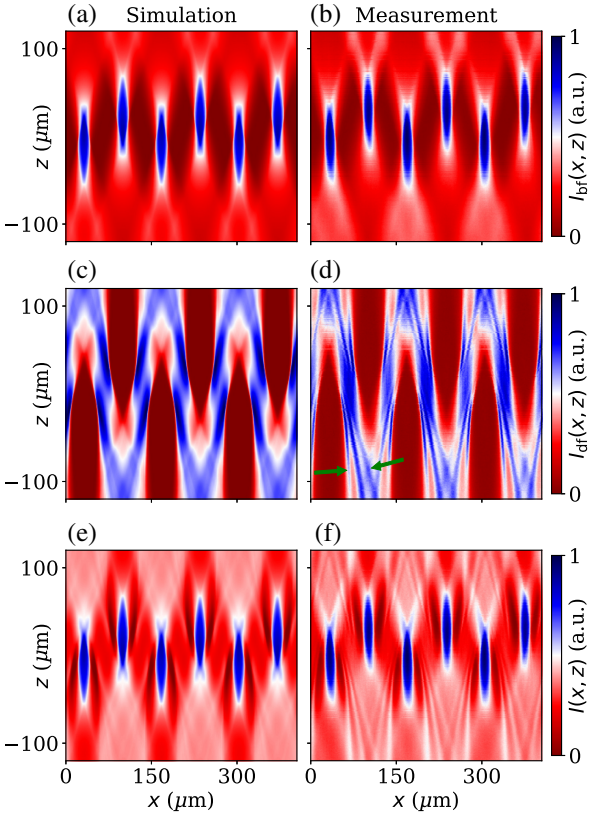

Fig. 6 (a), (c), (e) Simulated and (b), (d), (f) measured normalized intensity depth responses obtained from a sinusoidal surface profile of period length $L_x = 135$ μm and PV height $h = 19$ μm imaged by a 10×, NA = 0.45 focus variation microscope; (a), (b) for green LED bright-field illumination; (c), (d) for dark-field ring illumination with $\theta_{df,min} = 50°$ and $\theta_{df,max} = 79°$ with red LED light; and (e), (f) for combined dark- and bright-field illumination. The green arrows in (d) indicate an intensity modulation following from the dark-field ring light implemented by three separate LED ring arrangements in the measurement setup.

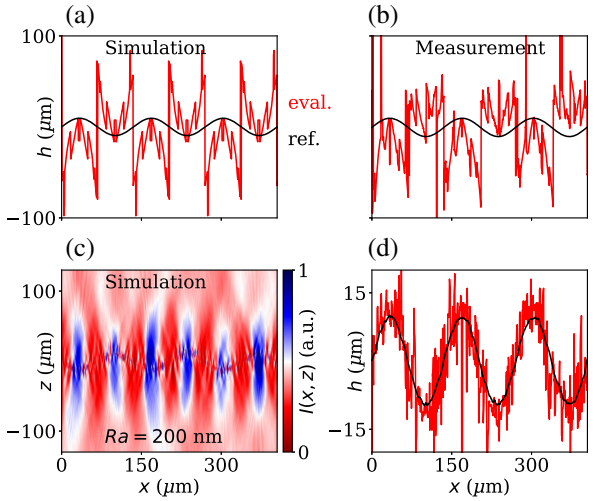

Fig. 7 Surface profiles (eval.) obtained from (a) simulated and (b) measured depth response signals depicted in Figs. 6(e) and 6(f), respectively. The reference profiles (ref.) are given by the nominal surface in the case of simulation and by tactile stylus measurement in the experimental case. (c) Normalized depth response signals obtained from the same sinusoidal surface profile shown as ref. In (a), superimposed with roughness of $R_a = 200$ nm for a combination of bright- and dark-field illumination. (d) The corresponding profile reconstruction and the nominal profile.

dark-field illumination. Comparing simulated and measured results, the measured result shows an additional modulation occurring as three bright stripes in the intensity, as marked by the green arrows in Fig. 6(d). In contrast to the simulation, where the ring light is assumed to be homogeneous, in practice the ring light is implemented in three layers, as reported by Xu et al.,[17] providing a simple explanation for the slight deviations between measurement and simulation.

Figures 6(e) and 6(f) present results obtained for a combination of bright- and dark-field illumination, where $I = I_{bf} + 2.2I_{df}$. Similar to the previous illumination configurations, simulated and measured results show good agreement despite slight deviations caused by the intensity distribution of the ring light, as explained in the discussion of the results obtained for dark-field illumination. Generally, due to the combination of both illumination types, light is collected from both, locally flat, specularly reflective, surface sections as well as from sloped parts of the surface profile.

Figures 7(a) and 7(b) display profiles obtained from the intensity signals shown in Figs. 6(e) and 6(f). The profile reconstruction is performed as described by Xu et al.[17] using five pixels to calculate the standard deviation as a measure of contrast. For reference (marked as ref. in Fig. 7), the nominal profile is shown in Fig. 7(a). In Fig. 7(b), the reference profile is obtained by the tactile stylus instrument MarSurf GD26. The microroughness of the measured profile resulted in an arithmetic mean value $R_a = 12$ nm (according to ISO 4287[55]) measured by AFM[18] and is neglected in the simulation.

Comparison of Figs. 7(a) and 7(b) shows good qualitative agreement. In both cases, the period length and the PV height can be extracted from the measured data with the accuracy provided by the method. However, the sinusoidal shape of the surface profile is reproduced neither by the measurement nor by the simulation. This significant deviation from the reference profile is caused by the fact that the surface shows a specular reflection, i.e., the microroughness superimposing the profile is very low. Therefore, the intensity obtained from the local areas of low surface slope is much greater compared to the intensity captured from light reflected at the sloped areas. Hence, the maximum contrast, which is related to the measured surface height as described by Xu et al.,[17] is detected from out-of-focus light reflected from the areas of low surface slope instead of the in-focus light from the sloped areas [see Figs. 6(e) and 6(f)]. Slight deviations between measurement and simulation again follow from different types of dark-field ring light.

In order to demonstrate the influence of microroughness on the measurement accuracy, Figs. 7(c) and 7(d) show simulated intensity signals [Fig. 7(c)] and the corresponding profile reconstruction [Fig. 7(d)] obtained from the same sinusoidal surface profile, but with a superimposed microroughness contribution of $R_a = 200$ nm using the combined bright- and dark-field illumination. Comparing Fig. 7(c) to intensity signals according to [Figs. 6(e) and 6(f)], the maximum intensities appearing at the peaks and valleys are still visible, but the sinusoidal shape of the profile can be obtained from the maximum local contrast and the sinusoidal profile is reproduced reliably.

Nonetheless, due to the limited axial resolution of FVM, the reconstructed profile still suffers from noise. The presented simulation model enables more detailed studies of FVM characteristics, which are beyond the scope of this paper.

In summary, simulated and measured results are in good agreement for all three types of illumination. Although a specular sinusoidal surface profile is not an intended measurement object for FVM measurements, it validates the simulation model and so allows one to identify any maladjustment of the microscope setup. However, as is well known, higher microroughness is required for reliable reconstruction of the surface topography based on FVM.

4 Conclusion

An accurate, quasianalytic modeling of the three most widespread optical techniques for surface topography measurement is presented. In order to model instrumental configurations providing high lateral and axial resolution as well as enabling measurements of steeply sloped surfaces, the scalar Kirchhoff modeling of scattering is extended to a vectorial treatment. Therefore, several rotations of the electric field during the focusing and scattering processes are to be considered. Simulations are performed and validated by comparison with measurement results for

- a Mirau interferometer of NA = 0.55, 50× magnification, and red LED illumination;
- a Linnik interferometer of NA = 0.95, 100× magnification, and royal blue LED illumination;
- a confocal microscope of NA = 0.95, 100× magnification, and cyan LED illumination;
- and a focus variation microscope of NA = 0.45, 10× magnification, with green LED bright-field illumination, red LED dark-field ring light, and a combination of both.

Measurements and simulations are obtained for sinusoidal surface profiles, as these profiles comply with the restrictions of the Kirchhoff approximation; they are often used for system characterization such as ITF estimation and can cause systematic deviations in measurement results due to the high-frequency components of sinusoidal phase gratings. For all of the studied measurement configurations, measured intensities as well as reconstructed profiles are reproduced accurately.

Since the modeling is based on analytic assumptions, simulation results are obtained in a timely fashion. However, for more complex surface profiles, which do not fulfill the requirements of the Kirchhoff approximation, the model is implemented in a way that Fourier coefficients can be calculated rigorously, while everything else remains unchanged.

In sum, an accurate model of most-used instruments for surface topography measurement is provided. The reliability of the modeling has been checked, especially with respect to measurement instruments of high lateral resolution for 2D surface profiles. However, an extension to 3D surfaces is straightforward. The model is simple, and fast, gives insight into physical mechanisms of imaging and scattering, and enables detailed studies of measurement performance for certain surface profiles and instrument configurations. Thus, the model can identify suitable measurement instruments and configuration for a certain application without great effort and cost.

In future studies, more quantitative comparisons, including an error estimation between simulated measured results, will be established. In addition, more detailed comparisons between scalar and vectorial models are of great interest, as most of the common simulation models are based on scalar theory. Moreover, the model can be used to investigate the limits, according to which surface topography measurement processes are subject to the linear transfer behavior of the instruments. In general, the model needs to be validated for more complex 2D and 3D surfaces by comparison to rigorously simulated as well as measured results. In addition to the rigorous models published by the authors (see Refs. 21 and 22), comparisons can be performed using more generally applicable commercial software, such as VirtualLab Fusion.[56]

5 Appendix

5.1 3D Surface Topographies

For clarity reasons, Figs. 3–5 display 2D profiles of 3D surface topographies measured with Mirau, Linnik, and confocal microscopes, respectively. Figure 8 shows 3D surface topography reconstructions for better credibility of the measurement results. The positions where the profiles are extracted are marked by black lines. Since the surface topography reconstruction of specular surfaces using FVM (Fig. 7) suffers from missing sloped areas, we refrain from showing the 3D surface topography here.

5.2 Comparison of the Scalar and Vectorial Approach

Differences between the scalar approach (Sec. 2.1.1) and the vectorial extension (Sec. 2.1.2) are demonstrated in the example of a 100× NA = 0.95 confocal microscope (see Sec. 3.2). Figure 9

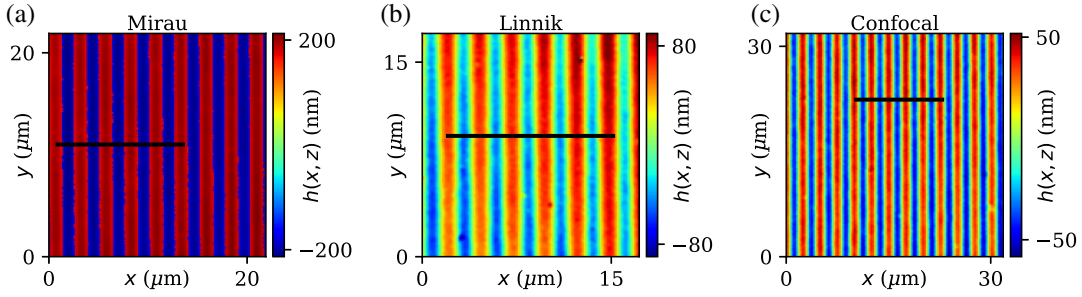

Fig. 8 Extracts of measured surface topographies obtained by a (a) Mirau and (b) Linnik interferometer as well as a (c) confocal microscope. The sections, where the profiles shown in Figs. 3–5 are extracted, respectively, are marked by black lines. The CSI results are obtained by phase analysis.

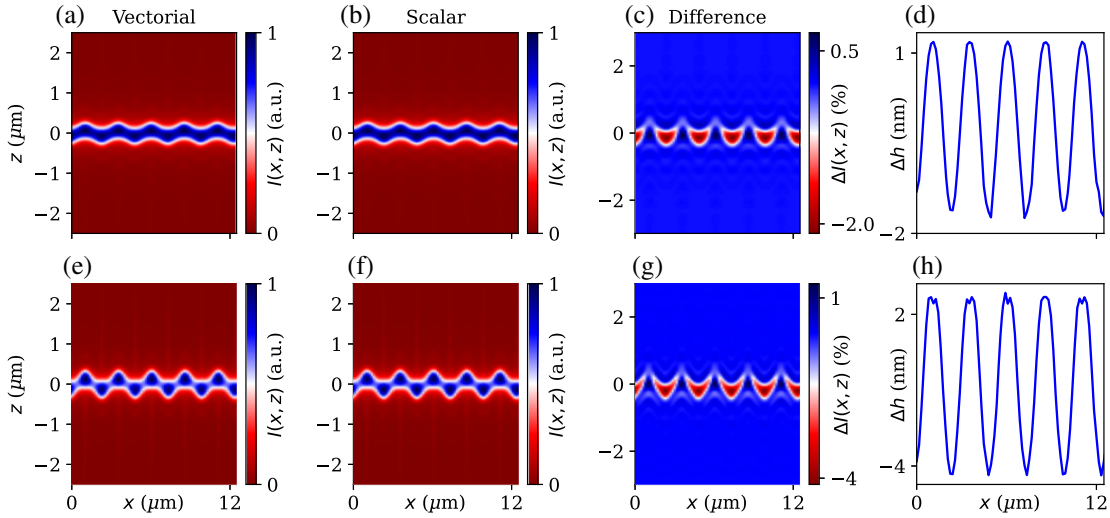

Fig. 9 Results obtained from a sinusoidal surface profile of period length $L_x = 2.5$ μm and PV height $h = 120$ nm (a)–(d) and $h = 240$ nm (e)–(h) considering a 100× NA = 0.95 confocal microscope with cyan LED illumination simulated using the (a), (e) vectorial and (b), (f) scalar approach. The differences between the intensities are displayed in (c) for $h = 120$ nm and (g) for $h = 240$ nm. The corresponding differences in the reconstructed height profiles are shown in (d) and (h), respectively.

displays image stacks simulated using the scalar [Figs. 9(b) and 9(f)] and the vectorial [Figs. 9(a) and 9(e)] approach for sinusoidal surfaces of $L_x = 2.5$ μm with two different PV heights, $h = 120$ nm [Figs. 9(a)–9(d)] and $h = 240$ nm [Figs. 9(e)–9(h)]. The differences in the image stacks are shown in Figs. 9(c) and 9(g), the differences between reconstructed height profiles in Figs. 9(d) and 9(h). It should be noted that Fig. 9(a) corresponds to Fig. 5(a). Considering the results for $h = 120$ nm, the difference between scalar and vectorial modeling is in the range of 2% for the image stacks ΔI and 2 nm for reconstructed profiles Δh. Since the amount of light in higher-diffraction orders increases with increasing surface height, the simulations are repeated for the doubled height of $h = 240$ nm. As expected, the differences increase [see Figs. 9(g) and 9(h)] to ∼4% for image stacks and 4 nm for reconstructed profiles. As a result, the usage of vectorial modeling plays a role in measurement instruments of high NA and becomes more important for objects scattering over broad angular ranges. Since the axial accuracy of confocal microscopes is in the range of nanometers and even lower for CSI instruments, an accurate modeling of the reconstructed height profiles is essential, especially for the development of virtual instruments intended to estimate measurement uncertainties.

Disclosures

The authors declare no conflict of interest.

Code and Data Availability

The data obtained and used in this contribution can be provided by the corresponding author upon request.

Acknowledgments

The authors gratefully acknowledge the financial support of the following research Projects (Nos. GZ: LE 992/14-3 and LE 992/18-1) by the Deutsche Forschungsgemeinschaft and the EMPIR program (project TracOptic, 20IND07) co-financed by the European Union's Horizon 2020 Research and Innovation Program.

References

1. P. de Groot, "Coherence scanning interferometry," in *Optical Measurement of Surface Topography*, R. Leach, ed., pp. 187–208, Springer, Berlin Heidelberg (2011).
2. P. Lehmann, S. Tereschenko, and W. Xie, "Fundamental aspects of resolution and precision in vertical scanning white-light interferometry," *Surf. Topogr. Metrol. Properties* **4**(2), 024004 (2016).
3. T. R. Corle and G. S. Kino, *Confocal Scanning Optical Microscopy and Related Imaging Systems*, Academic Press, San Diego (1996).
4. R. Artigas, "Imaging confocal microscopy," in *Optical Measurement of Surface Topography*, R. Leach, ed., pp. 237–286, Springer, Berlin Heidelberg (2011).
5. R. Danzl, F. Helmli, and S. Scherer, "Focus variation—a robust technology for high resolution optical 3D surface metrology," *Strojniski Vestnik/J. Mech. Eng.* **57**(3), 245–256 (2011).
6. L. Newton et al., "Areal topography measurement of metal additive surfaces using focus variation microscopy," *Addit. Manuf.* **25**, 365–389 (2019).
7. R. Leach, *Optical Measurement of Surface Topography*, Springer, Berlin Heidelberg (2011).
8. J. Schmit, K. Creath, and J. Wyant, "Surface profilers, multiple wavelength, and white light interferometry," in *Optical Shop Testing*, D. Malacara, ed., pp. 667–755, Wiley, New York (2007).
9. A. Harasaki and J. Wyant, "Fringe modulation skewing effect in white-light vertical scanning interferometry," *Appl. Opt.* **39**(13), 2101–2106 (2000).
10. P. de Groot et al., "Determination of fringe order in white-light interference microscopy," *Appl. Opt.* **41**(22), 4571–4578 (2002).
11. M. Conroy and J. Armstrong, "A comparison of surface metrology techniques," *J. Phys. Conf. Ser.* **13**(1), 458 (2005).
12. F. Mauch et al., "Improved signal model for confocal sensors accounting for object depending artifacts," *Opt. Express* **20**(18), 19936–19945 (2012).

13. C. Giusca et al., "Practical estimation of measurement noise and flatness deviation on focus variation microscopes," *CIRP Ann.* **63**(1), 545–548 (2014).
14. M. Rahlves, B. Roth, and E. Reithmeier, "Systematic errors on curved microstructures caused by aberrations in confocal surface metrology," *Opt. Express* **23**(8), 9640–9648 (2015).
15. W. Xie et al., "Signal modeling in low coherence interference microscopy on example of rectangular grating," *Opt. Express* **24**(13), 14283–14300 (2016).
16. A. Thompson et al., "Topography of selectively laser melted surfaces: a comparison of different measurement methods," *CIRP Ann.* **66**(1), 543–546 (2017).
17. X. Xu, S. Hagemeier, and P. Lehmann, "Outlier elimination in rough surface profilometry with focus variation microscopy," *Metrology* **2**(2), 263–273 (2022).
18. S. Hagemeier, "Comparison and investigation of various topography sensors using a multisensor measuring system," PhD thesis, University of Kassel (2022).
19. T. Pahl et al., "Vectorial 3D modeling of coherence scanning interferometry," *Proc. SPIE* **11783**, 117830G (2021).
20. T. Pahl, J. Breidenbach, and P. Lehmann, "Quasi-analytical and rigorous modeling of interference microscopy," in *Eur. Phys. J. Web of Conf.*, Vol. 266, p. 10013 (2022).
21. T. Pahl et al., "3D modeling of coherence scanning interferometry on 2D surfaces using FEM," *Opt. Express* **28**(26), 39807–39826 (2020).
22. T. Pahl et al., "Rigorous 3D modeling of confocal microscopy on 2D surface topographies," *Meas. Sci. Technol.* **32**(9), 094010 (2021).
23. J. Coupland et al., "Coherence scanning interferometry: linear theory of surface measurement," *Appl. Opt.* **52**(16), 3662–3670 (2013).
24. P. de Groot and X. Colonna de Lega, "Fourier optics modeling of interference microscopes," *J. Opt. Soc. Am. A* **37**(9), B1–B10 (2020).
25. R. Su and R. Leach, "Physics-based virtual coherence scanning interferometer for surface measurement," *Light Adv. Manuf.* **2**(1), 120–135 (2021).
26. P. Lehmann, M. Künne, and T. Pahl, "Analysis of interference microscopy in the spatial frequency domain," *J. Phys. Photonics* **3**(1), 014006 (2021).
27. W. Xie, "Transfer characteristics of white light interferometers and confocal microscopes," PhD thesis, University of Kassel (2017).
28. J. Coupland and J. Lobera, "Holography, tomography and 3D microscopy as linear filtering operations," *Meas. Sci. Technol.* **19**(7), 074012 (2008).
29. N. Nikolaev, J. Petzing, and J. Coupland, "Focus variation microscope: linear theory and surface tilt sensitivity," *Appl. Opt.* **55**(13), 3555–3565 (2016).
30. P. Lehmann and T. Pahl, "Three-dimensional transfer function of optical microscopes in reflection mode," *J. Microsc.* **284**(1), 45–55 (2021).
31. C. Sheppard, "Imaging of random surfaces and inverse scattering in the Kirchoff approximation," *Waves Random Media* **8**(1), 53 (1998).
32. H. Hooshmand et al., "Comparison of approximate methods for modelling coherence scanning interferometry," *Proc. SPIE* **12619**, 126190R (2023).
33. P. Lehmann, S. Hagemeier, and T. Pahl, "Three-dimensional transfer functions of interference microscopes," *Metrology* **1**(2), 122–141 (2021).
34. P. Lehmann, T. Pahl, and J. Riebeling, "Universal Fourier optics model for virtual coherence scanning interferometers," *Proc. SPIE* **12619**, 126190O (2023).
35. P. de Groot, "The instrument transfer function for optical measurements of surface topography," *J. Phys. Photonics* **3**(2), 024004 (2021).
36. M. Totzeck, "Numerical simulation of high-NA quantitative polarization microscopy and corresponding near-fields," *Optik* **112**(9), 399–406 (2001).
37. B. Richards and E. Wolf, "Electromagnetic diffraction in optical systems. II. Structure of the image field in an aplanatic system," *Proc. R. Soc. A* **253**(1274), 358–379 (1959).
38. P. Beckmann and A. Spizzichino, *The Scattering of Electromagnetic Waves from Rough Surfaces*, Artech House, Inc., Norwood, MA (1987).
39. W. Singer, M. Totzeck, and H. Gross, *Handbook of Optical Systems. Volume 2: Physical Image Formation*, John Wiley & Sons, Weinheim (2006).
40. J. A. Ogilvy and H. M. Merklinger, *Theory of Wave Scattering from Random Rough Surfaces*, IOP Publishing, Bristol (1991).
41. J. Ogilvy, "Wave scattering from rough surfaces," *Rep. Progr. Phys.* **50**(12), 1553 (1987).
42. E. Thorsos, "The validity of the Kirchhoff approximation for rough surface scattering using a Gaussian roughness spectrum," *J. Acoust. Soc. Am.* **83**(1), 78–92 (1988).
43. E. Thorsos and D. Jackson, "Studies of scattering theory using numerical methods," *Waves Random Media* **1**(3), S165 (1991).
44. T. Pahl et al., "Two-dimensional modeling of systematic surface height deviations in optical interference microscopy based on rigorous near field calculation," *J. Mod. Opt.* **67**(11), 963–973 (2020).
45. Rubert & Co Ltd., http://www.rubert.co.uk/reference-specimens/ (accessed 30 January 2023).
46. BudgetSensors Ltd., "Cantilever Tap190Al-G," (2023). https://www.budgetsensors.com/tapping-mode-afm-probe-long-cantilever-aluminum-tap190al.
47. S. Hagemeier, M. Schake, and P. Lehmann, "Sensor characterization by comparative measurements using a multi-sensor measuring system," *J. Sens. Sens. Syst.* **8**(1), 111–121 (2019).
48. W. Werner, K. Glantschnig, and C. Ambrosch-Draxl, "Optical constants and inelastic electron-scattering data for 17 elemental metals," *J. Phys. Chem. Ref. Data* **38**(4), 1013–1092 (2009).
49. F. Cheng et al., "Epitaxial growth of atomically smooth aluminum on silicon and its intrinsic optical properties," *ACS Nano* **10**(11), 9852–9860 (2016).
50. I. Abdulhalim, "Spatial and temporal coherence effects in interference microscopy and full-field optical coherence tomography," *Ann. Phys.* **524**(12), 787–804 (2012).
51. S. Tereschenko, "Digitale Analyse periodischer und transienter Messsignale anhand von Beispielen aus der optischen Präzisionsmesstechnik," PhD thesis, University of Kassel (2018).
52. R. Leach, "Some common terms and definitions," in *Optical Measurement of Surface Topography*, R. Leach, ed., pp. 15–22, Springer, Berlin Heidelberg (2011).
53. R. Shannon and J. Wyant, "Basic wavefront aberration theory for optical metrology," in *Applied Optics and Optical Engineering*, Vol. 11, J. Wyant and K. Creath, Eds., pp. 1–54, Academic Press, Inc., San Diego (1992).
54. P.-I. Schneider et al., "Reconstructing phase aberrations for high-precision dimensional microscopy," *Proc. SPIE* **12137**, 121370I (2022).
55. DIN EN ISO 4287, "Geometrical product specification (GPS)—surface texture: profile method—terms, definitions and surface texture parameters," Beuth Verlag, Berlin (2010).
56. LightTrans GmbH, "VirtualLab Fusion," https://www.lighttrans.com/products-services/virtuallab-fusion.html (accessed 14 December 2023).

Tobias Pahl received his master's degree in physics in 2018 from the University of Münster. He has been working as a research assistant and a PhD candidate in the Measurement Technology Group of the Department of Electrical Engineering and Computer Science at the University of Kassel since 2019. His main research interests are interference,

focus-variation, and confocal microscopes with high lateral resolution and their modeling.

Felix Rosenthal worked in the field of measurement technology at the University of Kassel, Germany, after completing his master's degree in physics. He has been a research assistant since 2023 and is working on his dissertation. His research focuses on the determination of the 3D transfer function of optical instruments and the processing of data.

Johannes Breidenbach completed his bachelor's degree in 2022. During his bachelor's thesis and his work as a student research assistant, he mainly dealt with the vectorial electromagnetic modeling of coherence scanning interferometry.

Corvin Danzglock received his master's degree in electrical engineering in 2023. His master's thesis dealt with efficient modeling of focus-variation microscopes. Since 2023, he works as a software engineer in an industrial company.

Sebastian Hagemeier has been working as a research assistant in the Department of Metrology at the University of Kassel, Germany, since October 2014. He completed his doctorate degree in engineering sciences in February 2022. His scientific work includes the comparison of the transfer behavior of various surface topography sensors in a multisensor measuring system. He is also working on the development and investigation of a fiber-coupled confocal-interferometric distance sensor for precise high-speed profilometry.

Xin Xu is a research employee in the Department of Messtechnik at the University of Kassel, Germany, since October 2019 and she did her doctorate meanwhile. She studied sensor system technology at the University of Applied Science, Germany and electrical communication engineering at the University of Kassel, Germany. She worked at an international company named USTER in China as a sensor engineer.

Marco Künne completed his master's degree in nanoscience in 2019. Since then, he has been working on his PhD at the University of Kassel in the field of optical metrology, specifically focusing on high-resolution Linnik interferometry. His academic research includes the development of precise optical setups as well as data processing and the work on new techniques for data evaluation.

Peter Lehmann studied physics at the University of Karlsruhe, Germany. He received his PhD in engineering at the University of Bremen in 1994 and received his habilitation degree in 2002. From 2001 to 2008, he coordinated research projects related to optical metrology in an industrial company. Since 2008, he has been a full professor and holds the chair in measurement technology at the Faculty of Electrical Engineering and Computer Science, University of Kassel, Germany.